Numerical model to predict wear of dynamically loaded plain bearings

Amandine Regis, Jean-Marc Linares, Santiago Arroyave-Tobón, Emmanuel Mermoz

Numerical model to predict wear of dynamically loaded plain bearings

Authors:
- Amandine Regis[a,b*]
- Jean-Marc Linares[a]
- Santiago Arroyave-Tobon[a]
- Emmanuel Mermoz[b]

a. Aix Marseille Univ, CNRS, ISM, Marseille, France
b. Airbus Helicopters, Aéroport International Marseille Provence, 13725 Marignane CEDEX, France
* Corresponding author, e-mail address: amandine.regis@univ-amu.fr

Abstract

Wear resistance of dynamic system components is a major challenge in aeronautics. According the usage of the aircraft, off-centred dynamic loads can appear on shafts when rotating bodies are unbalanced. In literature, most of the wear studies applied to plain bearing consider static loads centred in the contact area. This article presents a study on the wear of a plain bearing submitted to off-centred dynamic loads in order to look for a better mastering of service life of plain bearing for their usage in severe aeronautic conditions. Boussinesq's equations were used to compute the pressure distribution and Archard's law was used to calculate the wear. The wear coefficients of the running-in and stable wear stages were defined experimentally. The evolution over time of the maximum wear depth and the size of the contact zone were validated with experimental results. The perspective of this work is to feed digital twins of dynamic systems in order to predict wear according aircraft usage.

Keywords

Wear
Plain bearing
Unbalance load
Off-centred load
Running-in wear stage

1. Introduction

Wear is one of the main causes of damage and failure in mechanisms [1]. Wear rate increases with part misalignments [2] (asymmetric loading, clearance, assembly and/or manufacturing defaults) or dynamic loads [3]. Wear resistance of dynamic system components is a major challenge in aeronautics. In the case of helicopter's dynamic systems (Fig. 1a), off-centred dynamic loads can appear when rotating bodies are unbalanced (i.e. shaft bending, unbalanced mass). Fig. 1b represents an example of a bended transmission shaft supported by bearings. Fig. 1c presents a simplified representation of the plain bearing system under a dynamic load.

This article presents a study on the wear of a plain bearing submitted to off-centred dynamic loads in order to looks for a better mastering of service life of plain bearing for their usage in severe aeronautic conditions.

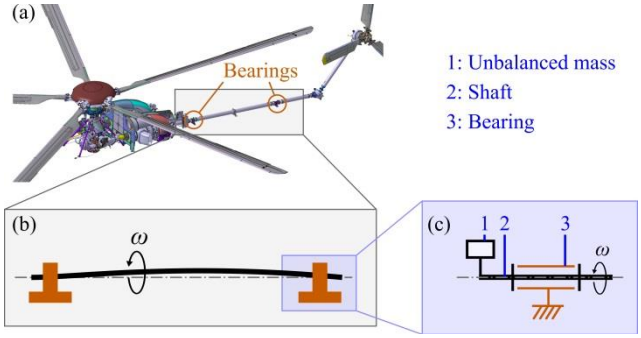

Fig. 1. (a) Helicopter dynamic systems; (b) Details of a bended transmission shaft supported by bearings; (c) Simplified representation of the plain bearing system under a dynamic load.

Several research works have been done on mechanical wear considering the running-in stage and the stable wear stage under different loading conditions.

Some works consider both the running-in and the stable wear stages in lubricated [4] or non-lubricated [5,6] mechanical systems. The running-in wear stage is characterized by a non-linear evolution of the rate of wear. Taking into account the running-in wear stage is difficult. Indeed, the friction coefficient, the wear coefficient, the temperature and the contact area evolve non-linearly in time [7]. Wear studies focusing on running-in were essentially done experimentally by studying the topographic evolution of the contact surface [8–11] and analytically by studying the influence of particles on wear [6,12].

The stable wear stage begins when parameters characterizing wear are stabilized. This phase represents the largest period of the system life and has been subjected to many studies. The stable wear stage was studied through different approaches: data-based and physics-based (Finite element models and specific models). The data-based approach rests on experimental tests to the better understand the wear phenomenon. The most used method is the implementation of pin-on-disc type tests. These tests allow to determine, among others, the wear coefficients [6,13,14]. Different test rigs were created to simulate wear cases of bearings of variable stator vane under engine-like condition [15] or to study the influence of the geometry of bearings on wear [16]. A test rig was also used with a design of experiments to study factors that influence the wear of bearings under mixed-lubrication conditions [17]. However, experimental tests are expensive and time consuming and some parameters, such as contact pressure, are difficult to measure directly.

To address that, physics-based approaches have been developed. Finite element analysis (FEA) with mesh updating was largely used to study wear. This approach allows to reduce the implementation time in wear studies compared to the data-based approach [18,19]. This method has been used to represent the behaviour of wear for tilted shafts under dynamic loads [20] or for bearing with complex bio-inspired geometry under static loads [21]. However, FEA are more time consuming than numerical models [22]. Some authors developed specific numerical models to predict wear of lubricated gears [4,23] or un-lubricated systems such as crossed steel wires [24,25], revolute joint in four-bar mechanism [22,26] or pin-on-disc configuration [14].

Wear phenomenon differs in function of the loading conditions. Fig. 2 depicts the difference of the position of the wear zones on the bearing and on the shaft for off-centred static and off-centred dynamic loads.

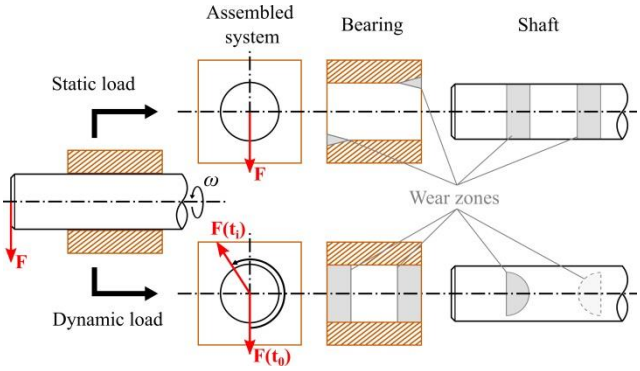

Fig. 2. Comparison of static and dynamic off-centred load cases for a plain bearing system when the rotating shaft is stopped axially.

Most of wear models consider static loads [21] or fretting conditions [5,19,27,28]. Models considering dynamic loads have been developed to predict wear of revolute joint in planar multibody system [22,26,29]. These models are useful in the case of planar mechanism where the rotational axes of the shaft and the bushing are parallels. In case of off-centred loads, the shaft tilts inside the bushing and

three-dimensional approaches are necessary. Schmidt and al. [20] computed wear of the titled shaft under dynamic load using finite element method.

This article presents the numerical model developed to predict the wear of the shaft and the bearings, for running-in and stable wear stage, under off-centred dynamic loading due to unbalanced mass. Results were validated by an experimental test rig.

2. Material and Methods

Wear of a plain bearing system under off-centred dynamic loads was studied to reproduce the operation conditions of unbalanced rotatory machinery. In order to reproduce the wear phenomenon, an experimental test rig was developed. A model is proposed to reproduce numerically this phenomenon. The experimental results allowed to determine the wear coefficients and to validate the model.

2.1. Experimental test rig

The test rig is illustrated by Fig. 3. A steel shaft OTMT 81001300 (item n°2 in Fig. 3) was rotationally guided by two bronze plain bearings SINT A50 (item n°3 in Fig. 3). The manufacturing tolerances of the bearings and the shaft are presented in Table 1. These parameters are assumed to be constant in this study and the influence of the variations are not taken into account. To create the dynamic load, an unbalanced mass (item n°1 in Fig. 3) was fixed at the shaft end. A double universal joint (item n°4 in Fig. 3) was used to link the shaft to the motor.

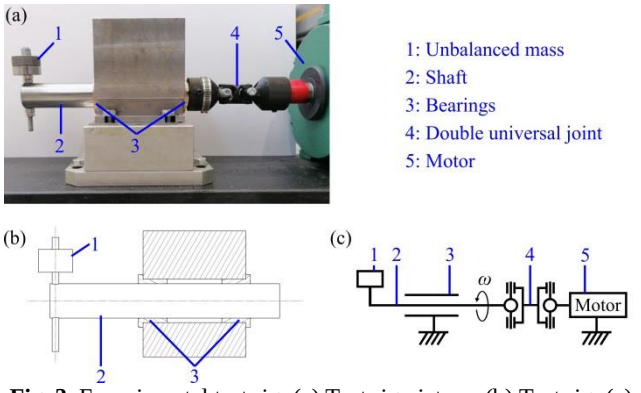

Fig. 3. Experimental test rig: (a) Test rig picture; (b) Test rig; (c) Kinematic chain to represent the test rig.

	Tolerance	Roughness (R_a)	Circularity
Bearings	H7	0.3 - 0.6	5 µm
Shaft	h6	0.3	6 µm

Table 1. Manufacturing tolerances of the bearings and the shaft.

Three unbalanced masses were used to create the dynamic load: 50, 75 and 100 g. The rotational speed of the shaft was fixed to 1000, 1250 or 1500 rpm. These values were defined to ensure enough centrifugal force to counteract gravity and keep a permanent contact between the shaft and the bearings. Table 2 presents the tests carried out. Test n°1 was used to estimate the wear coefficients. Then test n°2 and test n°3 were used to validate results of the analytical model. The wear of the shaft and the bearings was measured during each test.

Test number	m (g)	ω (rpm)
Test n°1: Calibration	75	1250
Test n°2: Prediction	50	1000
Test n°3: Prediction	100	1500

Table 2: Details of different tests done.

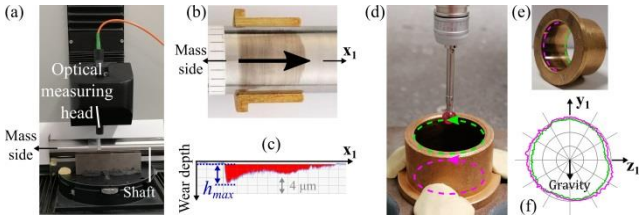

Fig. 4. Wear measurement methods (a-c) on shaft with a micromesure station and (d-f) on bearings with a coordinate measuring machine.

The geometry of the wear zone on the shaft was measured with a micromesure station (STIL Marposs, Micromesure 2) (Fig. 4a). This allowed obtaining a microtopography profile of the shaft (Fig. 4b). The measured profile was composed of an unworn portion to have a reference. An example of the obtained microtopography profile is presented in Fig. 4c. The difference between the best-fit line of the unworn reference portion and maximum depth corresponds to the maximum wear depth h_{max} of the shaft.

The geometry of the bearings was measured with a coordinate-measuring machine (Messwelk, MM 1004 E Trimesures) (Fig. 4d). We are interested in the maximum wear depth. This value is critical in the case of off-centred dynamic loads as it drives the maximum tilt of the shaft. Two circular paths inside the bearings were measured, at 1.5 mm from each end of the bearing. Each circular path was acquired with 200 points uniformly distributed. The maximum wear depth was estimated as the diameter variation of the best-fit circle of the current measure regarding the initial one. Fig. 4f presents an example of two measured circular paths (wear values were amplified to be visible).

2.2. Numerical wear model

The workflow of the proposed model used to predict wear is presented with Fig. 5. The input parameters of the model are the rotational speed of the shaft ω and the unbalanced mass m. Reaction forces at the two bearings are calculated in function of these parameters. Wear is calculated recursively considering the evolution of the contact area. Each iteration is composed of four main steps: computation of contact pressure and area with the

Boussinesq's equation, computation of wear volume with Archard's law, computation of wear depth and finally computation of cumulative wear. The simulation stops when the final time, fixed at 60 h, is achieved. These steps are detailed hereafter.

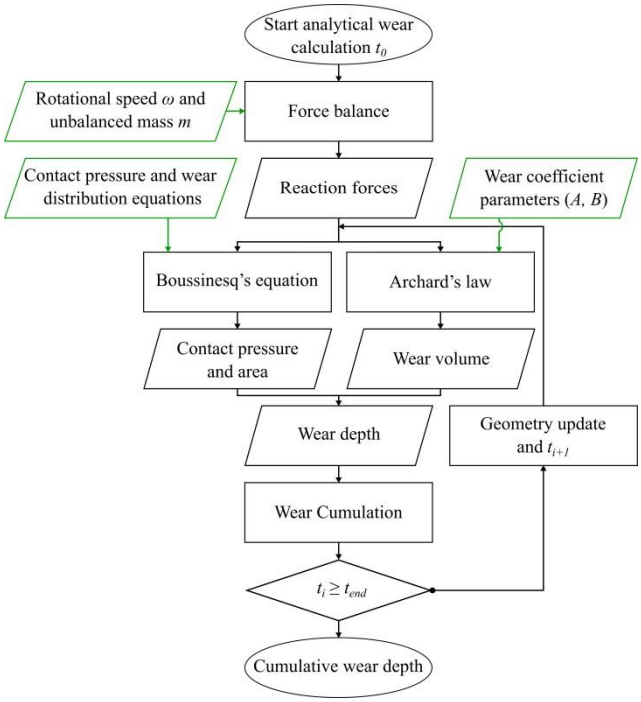

Fig. 5. Workflow of wear analytical method.

2.2.1. Force balance

For the resolution, some assumptions were made: bodies were supposed rigid and the effects of the clearance between the shaft and the bearing in the force balance were neglected. It was reported that friction affects the location of the wear zone but not the contact pressure distribution [30] so friction was neglected between the shaft and the bearing in the force balance.

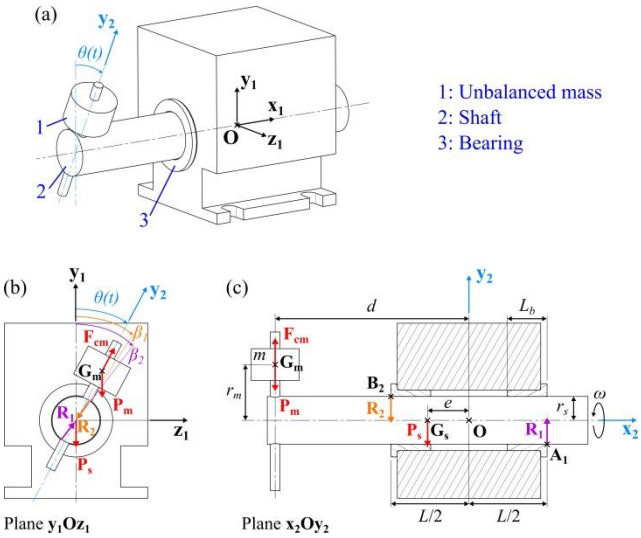

Fig. 6. Diagram of dynamic load case. (a) Isometric view; (b) Front view, plane $\mathbf{y_1Oz_1}$; (c) Side view, plane $\mathbf{x_2Oy_2}$.

The loads considered (Fig. 6) where: $\mathbf{P_s}$ the weight of shaft, $\mathbf{P_m}$ the weight of the unbalanced mass, $\mathbf{F_{cm}}$ the centrifugal force, $\mathbf{R_1}$ and $\mathbf{R_2}$ the contact reaction forces between shaft and bearings. By solving the force balance and projecting along the reference frame ($\mathbf{O}$, $\mathbf{x_1}$, $\mathbf{y_1}$, $\mathbf{z_1}$), the expression of contact reactions between shaft and bearings can be obtained:

$$R_1 = (1/2\mathrm{L})(F_{cm}{}^2(L-2d)^2 + (2eP_s - L(P_s+P_m) + 2dP_m)^2 - 2F_{cm}(L-2\mathrm{d})(L(P_s+P_m) - 2dP_m - 2eP_s)\cos\theta)^{1/2} \quad (1)$$

$$R_2 = (1/2L)(F_{cm}{}^2(L+2d)^2 + (2eP_s + L(P_s+P_m) + 2dP_m)^2 - 2F_{cm}(L+2d)(L(P_s+P_m) + 2dP_m + 2eP_s)\cos\theta)^{1/2} \quad (2)$$

where d is the positioning of the unbalanced mass, L the distance between outer faces of the bearings, e the distance between $\mathbf{O}$ and the centre of gravity of the shaft $\mathbf{G_s}$ on $\mathbf{x_2}$ axis and θ the position angle of the shaft. Fig. 7 shows the evolution of the reaction forces R_1 and R_2 for a revolution of the shaft for the parameters presented in Table 3**.**

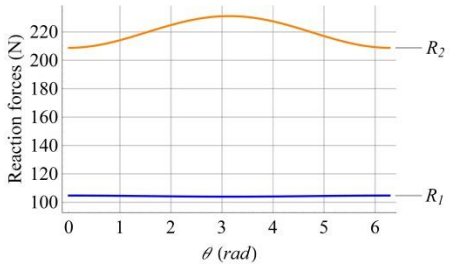

Fig. 7. Reaction force at interface between shaft and bearings for one revolution.

Parameters		Value
P_s	Weight of shaft (N)	10.53
P_m	Weight of unbalanced mass (N)	0.74
F_{cm}	Centrifugal force (N)	115.66
r_m	Eccentricity of the unbalanced mass (mm)	90
d	Positioning of the unbalanced mass (mm)	129
L	Distance between outer faces of the bearings (mm)	92
e	distance between $\mathbf{O}$ and $\mathbf{G_s}$ (mm)	37
L_b	Bearing length (mm)	25
r_s	External radius of shaft (mm)	14.985
r_b	Internal radius of bearing (mm)	15.005
E_s	Young's modulus of steel (GPa)	206
E_b	Young's modulus of bronze (GPa)	65
ν	Poisson's ratio	0.3

Table 3. Geometrical and material parameters of shaft and bearings.

2.2.2. Calculation of contact pressure and contact area

Boussinesq's equation was used to compute the contact area between the shaft and the bearings. Contacts were supposed frictionless and under normal pressure only. The Young's modulus of the steel shaft is named E_s and that of the bronze bearings E_b. An equivalent Young's modulus E_{eq} (Eq. (3)) and an equivalent shear modulus G_{eq} (Eq. (4)) were considered:

$$E_{eq} = \left(\frac{1-\nu^2}{E_s} + \frac{1-\nu^2}{E_b}\right)^{-1} \quad (3)$$

$$G_{eq} = \frac{E_{eq}}{2(1+\nu)} \quad (4)$$

where ν is the Poisson's ratio considered the same for both materials.

An equivalent radius was calculated in function of the radius of contact surfaces:

$$r_{eq} = \left(\frac{1}{r_s} + \frac{1}{r_b}\right)^{-1} \quad (5)$$

where r_s is the external radius of shaft and r_b the internal radius of bearing. Table 3 presents the geometrical and material parameters related to the shaft and the bearings.

Any point of the contact surface is defined by the coordinates (a, b) in the reference frame ($\mathbf{O_c}$, $\mathbf{x}$, $\mathbf{y_2}$, $\mathbf{z}$). The vectors of this reference frame are defined as follows: $\mathbf{x} = \mathbf{x_2}$ and $\mathbf{z} = \mathbf{z_2}^*$, where $\mathbf{z_2}^*$ is the axis of curvilinear coordinates of the cylindrical surface of the shaft (see Fig. 8b). The elastic strain $\delta(a,b)$ in the normal direction can be derived using Boussinesq's equations:

$$\delta(a,b) = \frac{1-\nu}{2\pi G_{eq}} \iint \frac{P(x,z)}{\sqrt{(a-x)^2+(b-z)^2}}\, dx\, dz \quad (6)$$

where $P(x,z)$ is the contact pressure field which was supposed to be linear in the plane with normal $\mathbf{z}$ and sinusoidal [16] in the plane with normal $\mathbf{x}$ (see Fig. 8). The boundary of the contact pressure field on the shaft was assumed to be parabolic. These three assumptions conduct to the following equations:

$$P(x,z) = P_{max}\left(1 - \frac{x}{L_c}\right)\cos\left(\frac{\pi\, z}{2 r_{eq}\varphi(x)}\right) \quad (7)$$

$$\varphi(x) = \pm \sin^{-1}\left(\sqrt{1 - \frac{x}{L_c}}\, \sin(\varphi_0)\right) \quad (8)$$

where P_{max} is the maximum contact pressure, L_c the contact length along the $\mathbf{x}$ axis, $\varphi(x)$ the half aperture angle of the contact surface and φ_0 the maximum half aperture angle (Fig. 8). By assuming small displacements, a linear expression of L_c can be obtained in function of the contact angle α and the maximum elastic strain δ_{max}:

$$L_c = (\delta_{max} + h_{max\_b} + h_{max\_s})/\alpha \quad (9)$$

$$\alpha = \tan^{-1}\left(\frac{2(r_b - r_s) + 2h_{max\_b} + h_{max\_s}}{L}\right) \quad (10)$$

where h_{max_b} and h_{max_s} are the maximum wear depths for the bearings and the shaft.

The expression of φ_0 can be deduced from geometrical relations (Fig. 8c):

$$\varphi_0 = \varphi(x=0) = \left|\tan^{-1}\left(\frac{C_1}{C_2 + (\Delta R + \delta_{max})}\right)\right| \quad (11)$$

where ΔR is the difference of radius and C_1 and C_2 two constants which depend on geometrical parameters:

$$\Delta R = r_b - r_s + h_{\max\_b} + h_{\max\_s} \quad (12)$$

$$C_1 = \sqrt{r_s{}^2 - (\Delta R + \delta_{max} + C_2)^2} \quad (13)$$

$$C_2 = \frac{r_s{}^2 - r_b{}^2 + (\Delta R + \delta_{max})^2}{2(\Delta R + \delta_{max})} \quad (14)$$

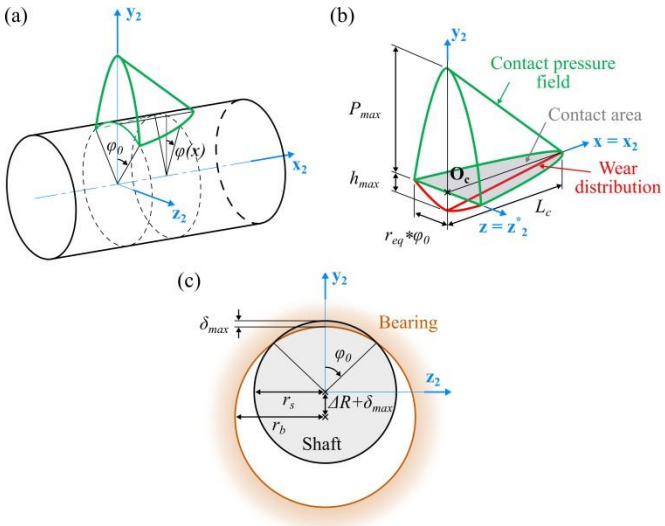

Fig. 8. Details of the contact between the shaft and the bearing: (a) contact pressure field on the shaft; (b) contact pressure field and wear distribution represented in curvilinear coordinates; (c) cross section of the maximal indentation between the shaft and the bearing.

In Eq. (6), if a and b are set to zero, the expression of the δ_{max} is obtained:

$$\delta_{max} = \delta(0,0) = \frac{1-\nu}{2\pi G_{eq}} P_{max} \int_{x=0}^{Lc} \int_{z=-r_{eq}\varphi(x)}^{r_{eq}\varphi(x)} \frac{\left(1-\frac{x}{L_c}\right) cos\left(\frac{\pi z}{2r_{eq}\varphi(x)}\right)}{\sqrt{x^2+z^2}} \, dz \, dx \quad (15)$$

where $\varphi(x)$ is obtained from Eq. (8).

The former system of equations cannot be solved analytically because of their non-linearities. Therefore, a numerical solution was adopted considering a finite number of angular positions of the shaft (spatial discretization). One revolution of the shaft was divided into N angular positions θ, where N is an integer. A sensitivity analysis was done to identify the influence of this spatial discretization.

The system of equations was solved by dichotomy method (Fig. 9). Each iteration computes the contact length L_c by means of Eq. (9), the maximum half aperture angle φ_0 by means of Eq. (11), the maximum contact pressure P_{max} by means of Eq. (15) and the residual difference ε by means of Eq. (16). The residual difference between the integral of the local forces over the contact area and the contact reaction force is minimized to guarantee the equilibrium:

$$\varepsilon = R(\theta) - \iint P(x,z)\, dx\, dz \quad (16)$$

where $R(\theta)$ is the normal reaction force applied between the shaft and the bearing for the angular position θ. If ε is smaller than a fixed error, parameters computed during the loop are accepted and computation stops.

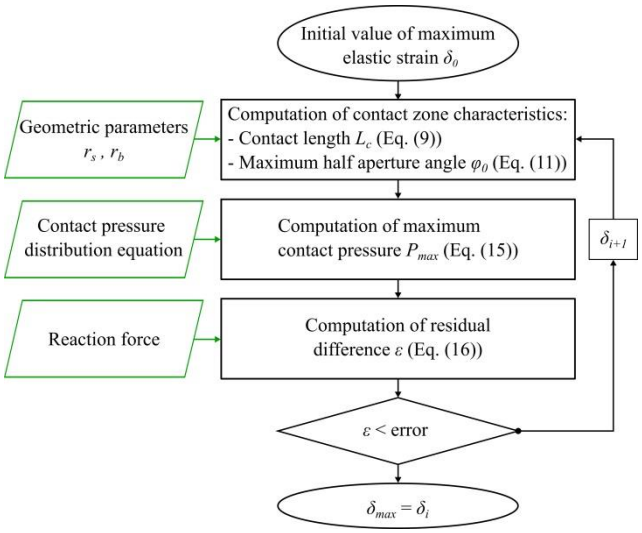

Fig. 9. Workflow of the calculation of contact pressure and contact area.

2.2.3. Wear volume calculation

Archard's law [31] was used to calculate the wear volume of the shaft and the bearings:

$$\Delta V(\theta) = K\, R(\theta) \Delta d \quad (17)$$

where $\Delta V(\theta)$ is the wear volume for the shaft or the bearings for the angular position θ and K the wear coefficient defined by $K = Kr/H$, where Kr is a dimensionless wear coefficient and H the material hardness. Δd is the sliding distance. For an angular portion, Δd can be calculated as:

$$\Delta d = 2\pi r_s / N \quad (18)$$

where N is the number of angular positions θ taken on one revolution (defined by the spatial discretization).

For the stable stage, wear has a linear evolution through time, so the stable stage wear coefficient named K_{lin} was supposed constant. For the running-in wear stage, the model proposed by Yang [6] was used to define the running-in wear coefficient K_{run}:

$$K_{run} = \frac{3A}{FL}(1 - e^{-BL}) \quad (19)$$

where F is the normal force fixed to the mean on one revolution of the reaction force R, A and B are constant coefficients determined experimentally and L is the total sliding distance for the entire time step defined by:

$$L = 2\pi r_s \omega \Delta t \quad (20)$$

where ω is the rotation speed of the shaft and Δt the time step.

For the shaft and the bearing wear coefficients were considered different. The coefficients A, B and K_{lin} were determined by means of experimental tests (Table 4).

	Shaft	Bearing
K_{lin} (MPa^{-1})	1.8 E-12	N*1.8 E-12
A (m^3)	2.8 E-11	1.25*N*2.8 E-11
B(m^{-1})	2 E-4	2 E-4

Table 4. Values of the wear coefficients.

2.2.4. Wear depth calculation

The shape of the wear distribution (represented in red in Fig. 8b) was assumed to be the same as that of the contact pressure (in green in Fig. 8b). Thus, the wear distribution $h(x,z)$ is given by the following equation:

$$h(x,z) = h_{max}\left(1 - \frac{x}{L_c}\right) \cos\left(\frac{\pi z}{2r_{eq}\varphi(x)}\right) \quad (21)$$

where h_{max} is the maximum wear depth. By integrating Eq. (21), the maximum wear depth can be calculated:

$$h_{\max}(\theta) = \frac{\Delta V(\theta)}{\int_{x=0}^{L_c} \int_{z=-r_{eq}\varphi(x)}^{r_{eq}\varphi(x)} \left(1-\frac{x}{L_c}\right) cos\left(\frac{\pi z}{2r_{eq}\varphi(x)}\right) dz\, dx} \quad (22)$$

where $h_{max}(\theta)$ is the maximum wear depth for the shaft or the bearings related to an angular position θ.

2.2.5. Cumulative wear depth

Due to the type of the studied dynamic loading, the same zone of the shaft slid around the entire inner face of the bearings. Therefore, the way to calculate the cumulative wear depth of the shaft and the bearings was different.

For the shaft, the wear depths calculated for each angular positions θ were added to have the wear depth on one revolution $h^*_{max\_s}$:

$$h^*_{max\_s} = \sum_{i=1}^{N} h_{max\ \_s}(\theta_i) \quad (23)$$

where h_{max_s} was calculated from Eq. (22) using the wear coefficient of the shaft (Table 4).

For the bearings, the wear was located all around the inner face. So, the wear depth for each angular portion is different and was calculated considering the related reaction force and the wear coefficients of the bearings (Table 4).

To obtain the cumulative wear depths for the shaft and the bearings for the time step, the wear depth for one revolution was multiplied by the number of revolutions done during the time step.

2.2.6. Geometry update

Because of wear, the clearance between the shaft and the bearings increases. This is why the wear depth is taken into account to compute the radius difference ΔR (Eq. (12)), the contact angle α (Eq. (10)) and the contact length L_c (Eq. (9)).

2.3. Confidence intervals

Monte Carlo's method was used to compute confidence intervals of the results. Input parameters of the proposed model were varied following a normal distribution. The variations are mainly related to uncertainties of the measuring process. Table 5 presents these parameters, the mean and the assumed variation.

Parameters	Mean	Variation
Unbalanced mass m (g)	50, 75, 100	± 10
Rotational speed ω (rpm)	1000, 1250, 1500	± 50
Eccentricity of m (mm)	90	± 2
Positioning of m (mm)	129	± 2
Radius diff. ΔR (µm)	15	± 10
Coefficient A	2.8 E-11	± 0.14 E-11
Coefficient B	2 E-4	± 0.10 E-4

Table 5. Input parameters of Monte Carlo method.

Confidence intervals were assumed as three times the standard deviation. Table 6 gives values that characterize confidence interval at final time for six outputs of the developed model for the test n°1.

	Mean	Standard deviation
Max. wear depth on shaft (µm)	5.65	0.66
Max. wear depth on bearing (µm)	6.18	0.74
Max. contact pressure (MPa)	2.61	0.23
Contact length (mm)	23.16	1.27
Max. half aperture angle (deg)	56.57	1.79
Contact area (mm^2)	81.21	6.60

Table 6. Outputs of Monte Carlo computations for test n°1 at final time.

3. Results and discussion

All results presented hereafter are for the mass-side contact zone.

3.1. Determination of the wear coefficients

The determination of the wear coefficient was done for ω = 1250 rpm and m = 75 g (test n°1 in Table 2). Wear coefficients were calculated to include the experimental results in the calculated confidence intervals. Fig. 10 shows the evolution of the maximum wear depth through time for the shaft (Fig. 10a) and the bearing (Fig. 10b). This figure shows: the experimental results from the test rig (red and dark green dots and triangles), the numerical result from the model developed (purple and green dotted line) and the confidence intervals (light grey zone). The repeatability was evaluated for test n°1 by doing it twice. All the measures of the two tests (dots for the first test and triangles for the second one in Fig. 10) are inside the confidence interval so the repeatability of the experiments was supposed valid for test n°2 and test n°3. It is known that the wear coefficient depends on many parameters such as speed, load or temperature. In this work, the variability of the wear coefficient was considered in the uncertainty analysis (Section 2.3 and Table 5).

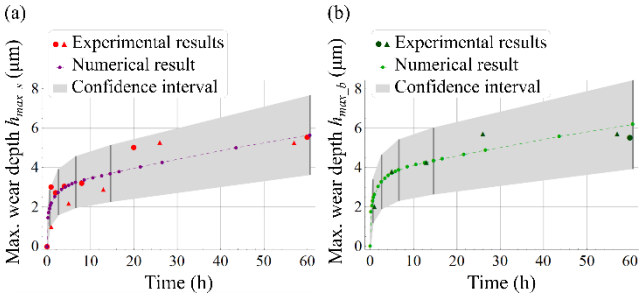

Fig. 10. Maximum wear depth through time for test n°1for (a) the shaft and (b) the bearing.

Validation of the developed model

The results predicted by the developed model under different loading conditions (ω and m) and

using the computed wear coefficients were validated experimentally.

For test n°2, the rotational speed ω was higher (1500 rpm) and the unbalanced mass m heavier (100 g) than test n°1. Fig. 11 presents the evolution of the maximum wear depth for the shaft (Fig. 11a) and the bearing (Fig. 11b). All experimental results of wear depth of the shaft (red dots in Fig. 11a) and the bearing (dark green star in Fig. 11b) are inside the confidence intervals and close to the numerical result. Fig. 12 shows the evolution through time of the maximum contact pressure (Fig. 12a), the contact area (Fig. 12b), the contact length (Fig. 12c) and the maximum half aperture angle (Fig. 12d) for test n°2.

The different stages of the wear process can be seen in Fig. 11 and Fig. 12. The running-in wear stage is until time of 6 h and then there is the stable wear stage where the evolution is almost linear. However, on Fig. 12b and Fig. 12c there is a slope discontinuity appearing at about 26 h. This change of slope is due to the limit in the contact length imposed by the bearing geometry (length L_b). Once the contact length achieves this limit, it stays constant and directly impacts the evolution of the contact area (Fig. 12b).

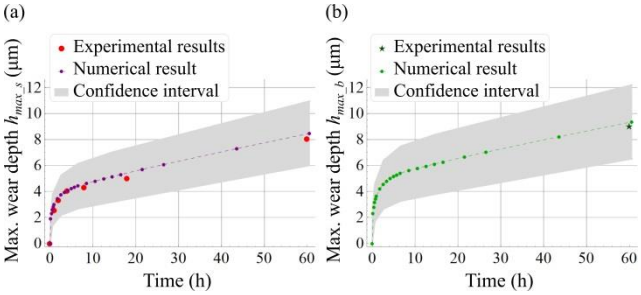

Fig. 11. Maximum wear depth through time for (a) the shaft and (b) the bearing for test n°2.

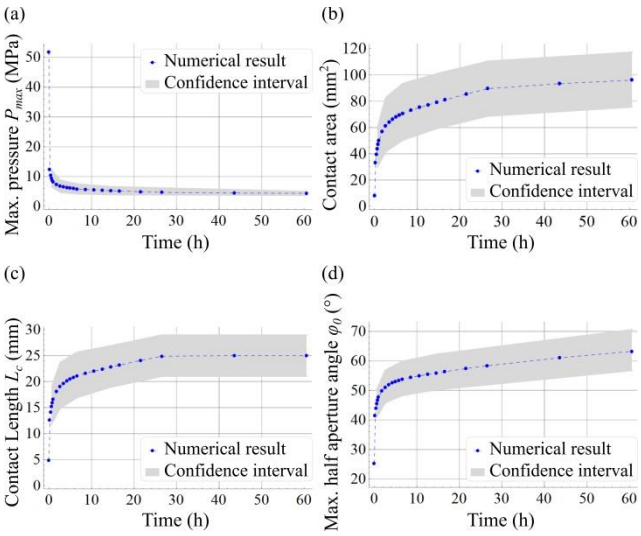

Fig. 12. Evolution of the contact field characteristics through time for test n°2: (a) the maximum contact pressure, (b) the contact area, (c) the contact length and (d) the maximum half aperture angle.

Test n°3 was realized with a lower rotational speed ω (1000 rpm) and a lighter unbalanced mass m (50 g) than test n°1. Fig. 13 and Fig. 14 present the evolution through time of the maximum wear depth for the shaft (Fig. 13a), the maximum wear depth for the bearing (Fig. 13b), the maximum contact pressure (Fig. 14a), the contact area (Fig. 14b), the contact length (Fig. 14c) and the maximum half aperture angle (Fig. 14d). All experimental results of the wear depth for this test are inside the confidence intervals of the predicted results. However, it can be noticed that the gap between the experimental and the numerical results for the wear depth of the shaft (Fig. 13a) increases with time. At time of 60 h this difference reaches up to 62 %. This difference can be related with the fact that measured wear depth was relatively small regarding the precision of the measuring tool.

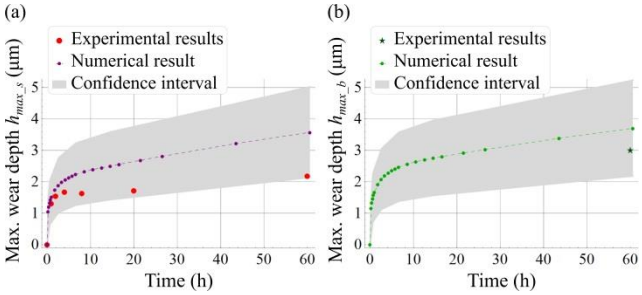

Fig. 13. Maximum wear depth through time for (a) the shaft and (b) the bearing for test n°3.

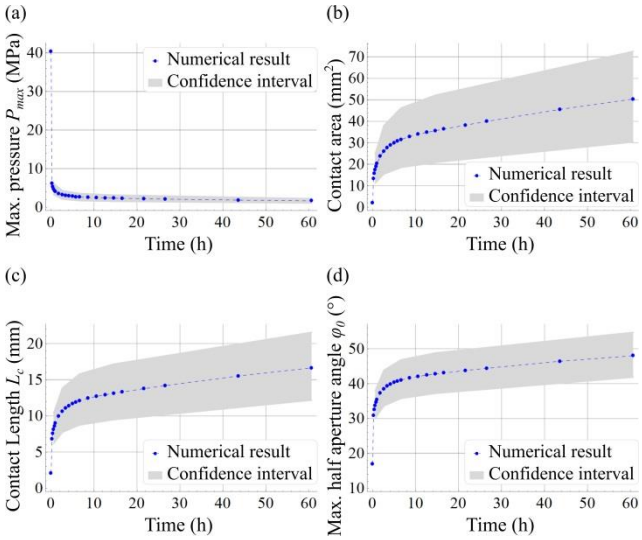

Fig. 14. Evolution of the contact field characteristics through time for test n°3: (a) the maximum contact pressure, (b) the contact area, (c) the contact length and (d) the maximum half aperture angle.

3.2. Comparison of the results with other works

Obtained numerical results cannot be quantitatively compared to other works because similar cases (in terms materials properties and

loading conditions) have not been reported in the literature. Nevertheless, the evolution wear can be compared from a qualitative point of view. In [27] [14] and [25] a similar evolution regarding our results of the wear thought time have been reported. Other authors [19,25,27,32] have also observed a rapid decrease of the contact pressure at the very beginning of the wear process.

3.3. Worn geometry of the bearing

Due to the type of the studied dynamic loading, the entire inner face of the bearings is worn. The developed model is able to predict the worn geometry of the bearings and the numerical results have been compared to the experimental results. Fig. 15 shows the final worn profile (in green) of the bearings compared to the reference profile (in black). For both results, numerical (Fig. 15a) and experimental (Fig. 15b), the wear is not uniform on the whole inner face of the bearing. The maximum wear depth of the bearing (red line in Fig. 15) is not located at the same place. For the numerical result, the maximum wear depth is aligned with the $\mathbf{y_1}$-axis, whereas for the experimental result, it is shifted. The reason of this difference is related with the fact of not taking into account friction in the contact calculation. Indeed, it was reported that frictional contact contributes to shift the location of wear but does not influence the pressure distribution [30].

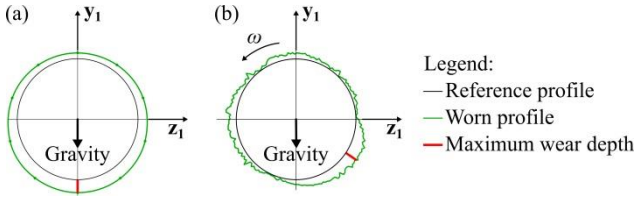

Fig. 15. The profile of the wear for the bearing after 60 h with (a) the developed model and (b) the test rig (to be visible, deformations have been amplified).

3.4. Computation time comparison

The advantage of using the developed model is to be less time consuming than FEA. The developed model needed about 22 minutes to simulate 4.5E6 cycles with a standard laptop (2.7 GHz Intel Core i7 processor and 16 GB of RAM). Authors working with FEA to predict wear reported longer computational time (Table 7).

Ref.	Number of cycles	Computational time	CPU characteristics
[27]	18 000	24 hours	Not reported
[33]	408 000	3.4 hours	Processor: 2.0 GHz Intel Pentium RAM: 2.0 GB
[34]	Not reported	2.2 hours	Processor: 3.6 GHz Intel Core i7 RAM: 16 GB

Table 7. Computational time for FEA models predicting wear from literature.

3.5. Influence of the discretization method

Several tests were done to analyse the influence of spatial and temporal discretization on maximum wear depth of the shaft and the bearings.

(i) Spatial discretization

From a sensitivity analysis, it was found that N had little influence on maximum wear depth results. The difference on the calculated maximum wear depth when increasing N = 4 to N = 28 was about 0.02%. However, the computational time increased of about 20%.

(ii) Temporal discretization

In the stable wear stage, the size of the time step had low influence on final results. Multiplying by two the time step (from 10 h to 20 h) in stable wear stage induced a difference of 0.8% on the final maximum wear depth of the shaft. In the running-in wear stage, the size of the time step had more influence on the maximum wear depth. Multiplying by two the time step (from 0.1 h to 0.2 h) during the first hour of simulation induced a difference of 1.4% on final maximum wear depth. By using smaller time steps, the total computational time increased: from 20 to 30 iterations in total increased the computational time of about 50%.

Based on these conclusions, a non-uniform discretization of time was made for all the computations results in this paper. During the running-in wear stage time step of 0.2 h until 1 h and 0.8 h between 1 h and 6 h were taken. It increased when it approached stable wear stage with a time step of 2 h between 6 h and 15 h. And then, time step of 5 h between 15 h and 25 h and 17 h between 25 h and 60 h were used.

4. Conclusion

In this work, a model to predict the wear of a plain bearing system under dynamic off-centred loads was developed. The model predicts the characteristics of the pressure and the wear fields: maximum wear depths of the shaft and the bearings, maximum contact pressure, contact length and contact area. In this work, the rotational speed was constant for each test. In other case studies, the developed model can be used to predict wear with non-constant rotational speed. It can be also enhanced to consider frictional contacts to better determine the location of maximum wear depth on bearing as represented in Fig. 15.

The dynamic off-centred loading considered was represented by an unbalanced mass fixed to a shaft. This configuration of loads generates a wear located always on the same area of the shaft but distributed

on the entire inner face of the bearings. This spatial repartition of wear was taken into account.

A test rig was used to determine the wear coefficients of the shaft and the bearings. The test rig was also used to validate the model but with different speed and loads conditions. The experimental results of the wear depths of the shaft and the bearings were good agreement with the model results.

These kinds of specific numerical models are less time consuming than finite element analysis, so it represents a good alternative for describing the wear progression in the frame of digital twin applications for helicopters.

Acknowledgements

This work was supported by Airbus Helicopters, Aix-Marseille University and ANRT (Association Nationale pour la Recherche et la Technologie) by the grant n° 2019/1242. The experimental devices were founded by: European Community, French Ministry of Research and Education and Aix-Marseille Conurbation Community.

References

[1] V.L. Popov, Contact Mechanics and Friction, Springer Berlin Heidelberg, Berlin, Heidelberg, 2010. https://doi.org/10.1007/978-3-642-10803-7.

[2] J. Jang, M. Khonsari, On the Characteristics of Misaligned Journal Bearings, Lubricants. 3 (2015) 27–53. https://doi.org/10.3390/lubricants3010027.

[3] S. Strzelecki, Z. Towarek, Effect of Shaft Unbalance on the Operation of Worm Gear Rolling Bearings, Key Eng. Mater. 293–294 (2005) 441–450. https://doi.org/10.4028/www.scientific.net/KEM.293-294.441.

[4] S. Akbarzadeh, M.M. Khonsari, Experimental and theoretical investigation of running-in, Tribol. Int. 44 (2011) 92–100. https://doi.org/10.1016/j.triboint.2010.09.006.

[5] A. Cruzado, M. Hartelt, R. Wäsche, M.A. Urchegui, X. Gómez, Fretting wear of thin steel wires. Part 1: Influence of contact pressure, Wear. 268 (2010) 1409–1416. https://doi.org/10.1016/j.wear.2010.02.017.

[6] L.J. Yang, A test methodology for the determination of wear coefficient, Wear. 259 (2005) 1453–1461. https://doi.org/10.1016/j.wear.2005.01.026.

[7] P.J. Blau, On the nature of running-in, Tribol. Int. 38 (2005) 1007–1012. https://doi.org/10.1016/j.triboint.2005.07.020.

[8] Y.-R. Jeng, Z.-W. Lin, S.-H. Shyu, Changes of Surface Topography During Running-In Process, J. Tribol. 126 (2004) 620–625. https://doi.org/10.1115/1.1759344.

[9] G. Zhang, X. Liu, W. Lu, Comprehensive evaluation of surface topography in running-in wear process, in: S. Ye, Y. Fei (Eds.), Proc. SPIE, Guiyang, China, 2013. https://doi.org/10.1117/12.2041643.

[10] S.K.R. Chowdhury, H. Kaliszer, G.W. Rowe, An analysis of changes in surface topography during running-in of plain bearings, Wear. 57 (1979) 331–343.

[11] O.A. Zambrano, E.C. Muñoz, S.A. Rodríguez, J.J. Coronado, Running-in period for the abrasive wear of austenitic steels, Wear. 452–453 (2020) 203298. https://doi.org/10.1016/j.wear.2020.203298.

[12] Z. Zhang, L. Zhang, Y.-W. Mai, The running-in wear of a steel/Sic,-Al composite system, Wear. 194 (1996) 38–43.

[13] P. Põdra, S. Andersson, Simulating sliding wear with finite element method, Tribol. Int. 32 (1999) 71–81. https://doi.org/10.1016/S0301-679X(99)00012-2.

[14] V. Hegadekatte, N. Huber, O. Kraft, Modeling and simulation of wear in a pin on disc tribometer, Tribol. Lett. 24 (2006). https://doi.org/10.1007/s11249-006-9144-2.

[15] T. Wollmann, S. Nitschke, T. Klauke, T. Behnisch, C. Ebert, R. Füßel, N. Modler, M. Gude, Investigating the friction, wear and damage behaviour of plain bearing bushes of the variable stator vane system, Tribol. Int. 165 (2022) 107280. https://doi.org/10.1016/j.triboint.2021.107280.

[16] R.S. Colbert, L.A. Alvarez, M.A. Hamilton, J.G. Steffens, J.C. Ziegert, D.L. Burris, W.G. Sawyer, Edges, clearances, and wear: Little things that make big differences in bushing friction, Wear. 268 (2010) 41–49. https://doi.org/10.1016/j.wear.2009.06.030.

[17] A. Ramamohana Rao, P.V. Mohanram, A study of wear characteristics of journal bearings operating under mixed-lubrication conditions, Wear. 172 (1994) 11–22. https://doi.org/10.1016/0043-1648(94)90294-1.

[18] A. Rezaei, W. Van Paepegem, P. De Baets, W. Ost, J. Degrieck, Adaptive finite element simulation of wear evolution in radial sliding bearings, Wear. 296 (2012) 660–671. https://doi.org/10.1016/j.wear.2012.08.013.

[19] A. Cruzado, M.A. Urchegui, X. Gómez, Finite element modeling and experimental validation of fretting wear scars in thin steel wires, Wear. 289 (2012) 26–38. https://doi.org/10.1016/j.wear.2012.04.018.

[20] A.A. Schmidt, T. Schmidt, O. Grabherr, D. Bartel, Transient wear simulation based on three-dimensional finite element analysis for a dry running tilted shaft-bushing bearing, Wear. 408–409 (2018) 171–179. https://doi.org/10.1016/j.wear.2018.05.008.

[21] D. Sysaykeo, J.-M. Linares, E. Mermoz, Wear Behavior of a Bio-inspired Bearing for off-center Loads, J. Bionic Eng. 17 (2020) 1251–1262. https://doi.org/10.1007/s42235-020-0107-3.

[22] P. Flores, Modeling and simulation of wear in revolute clearance joints in multibody systems, Mech. Mach. Theory. 44 (2009) 1211–1222. https://doi.org/10.1016/j.mechmachtheory.2008.08.003.

[23] S. Akbarzadeh, M.M. Khonsari, Prediction of Steady State Adhesive Wear in Spur Gears Using the EHL Load Sharing Concept, J. Tribol. 131 (2009) 024503. https://doi.org/10.1115/1.3075859.

[24] Y. Chen, F. Meng, X. Gong, Interwire wear and its influence on contact behavior of wire rope strand subjected to cyclic bending load, Wear. 368–369 (2016) 470–484. https://doi.org/10.1016/j.wear.2016.10.020.

[25] Y. Chen, F. Meng, Numerical study on wear evolution and mechanical behavior of steel wires based on semi-analytical method, Int. J. Mech. Sci. 148 (2018) 684–697. https://doi.org/10.1016/j.ijmecsci.2018.09.030.

[26] X. Lai, H. He, Q. Lai, C. Wang, J. Yang, Y. Zhang, H. Fang, S. Liao, Computational prediction and experimental validation of revolute joint clearance wear in the low-velocity planar mechanism, Mech. Syst. Signal Process. 85 (2017) 963–976. https://doi.org/10.1016/j.ymssp.2016.09.027.

[27] I.R. McColl, J. Ding, S.B. Leen, Finite element simulation and experimental validation of fretting wear, Wear. 256 (2004) 1114–1127. https://doi.org/10.1016/j.wear.2003.07.001.

[28] J. Madge, S. Leen, P. Shipway, A combined wear and crack nucleation–propagation methodology for fretting fatigue prediction, Int. J. Fatigue. 30 (2008) 1509–1528. https://doi.org/10.1016/j.ijfatigue.2008.01.002.
[29] S. Mukras, N.H. Kim, N.A. Mauntler, T.L. Schmitz, W.G. Sawyer, Analysis of planar multibody systems with revolute joint wear, Wear. 268 (2010) 643–652. https://doi.org/10.1016/j.wear.2009.10.014.
[30] L. Mattei, F. Di Puccio, Wear Simulation of Metal-on-Metal Hip Replacements With Frictional Contact, J. Tribol. 135 (2013) 021402. https://doi.org/10.1115/1.4023207.
[31] J.F. Archard, Contact and Rubbing of Flat Surfaces, J. Appl. Phys. 24 (1953) 981–988. https://doi.org/10.1063/1.1721448.
[32] D.E. Sander, H. Allmaier, H.H. Priebsch, F.M. Reich, M. Witt, A. Skiadas, O. Knaus, Edge loading and running-in wear in dynamically loaded journal bearings, Tribol. Int. 92 (2015) 395–403. https://doi.org/10.1016/j.triboint.2015.07.022.
[33] S. Mukras, N.H. Kim, W.G. Sawyer, D.B. Jackson, L.W. Bergquist, Numerical integration schemes and parallel computation for wear prediction using finite element method, Wear. 266 (2009) 822–831. https://doi.org/10.1016/j.wear.2008.12.016.
[34] C. Curreli, F. Di Puccio, L. Mattei, Application of the finite element submodeling technique in a single point contact and wear problem, Int. J. Numer. Methods Eng. 116 (2018) 708–722. https://doi.org/10.1002/nme.5940.